Earth and Planetary Science Letters 591 (2022) 117593

Contents lists available at ScienceDirect

Earth and Planetary Science Letters

www.elsevier.com/locate/epsl

# Rupture styles linked to recurrence patterns in seismic cycles with a compliant fault zone

Shiying Nie *, Sylvain Barbot

*Department of Earth Sciences, University of Southern California, 3651 Trousdale Pkwy, Los Angeles, CA 90089, USA*

ARTICLE INFO

*Article history:*
Received 3 March 2022
Received in revised form 27 April 2022
Accepted 6 May 2022
Available online xxxx
Editor: R. Bendick

*Keywords:*
seismic cycle
numerical model
fault friction
compliant zone
pulse-like rupture
aftershocks

ABSTRACT

Seismic cycles emerge in a broad range of rupture styles, from slow-slip events to pulse-like earthquake sequences. Meanwhile, large earthquakes in paleoseismic and instrumental catalogues exhibit various recurrence patterns going from periodic to chaotic cycles with characteristic or dissimilar ruptures. The potential connection between these observations is still poorly known. Here, we investigate the link between rupture styles and recurrence patterns in quasi-dynamic models of seismicity in two-dimensional faults embedded in a compliant zone, exploring a wide range of frictional and fault zone properties. The recurrence patterns evolve from purely periodic to multiple-periodic time- and slip-predictable cycles, to chaotic sequences of super-cycles with full and partial ruptures with an increasing number of aftershocks. This transition is accompanied by changes of rupture styles from crack-like to pulse-like ruptures. These behaviors can be obtained either by a more compliant fault zone or a reduced characteristic weakening distance of friction. The effects of the compliant zone and other physical characteristics can be conflated into a single non-dimensional number, such that seismic cycles with similar behaviors can be obtained with or without a compliant fault zone in quasi-dynamic simulations. The connection between recurrence patterns and rupture styles implies that the paleoseismic record can bring useful constraints to rupture characteristics and fault zone properties.



## 1. Introduction

The seismic cycle is maintained by the large-scale motion of tectonic plates that slowly reload faults after a rupture (Reid, 1910). The recurrence pattern of large earthquakes is controlled by many factors, including the structural fabric (Wesnousky, 1988, 2006; Dolan et al., 2016), frictional properties (Leeman et al., 2016; Veedu et al., 2020), and tectonic assembly (Gauriau and Dolan, 2021) of the host fault, modulated by static and remote triggering (King et al., 1994; Freed and Lin, 2001; Gomberg and Johnson, 2005). Earthquake sequences on a given fault segment sometimes approach the time-predictable and slip-predictable models based on a fixed yield strength or a coseismic basal friction, respectively (Bufe et al., 1977; Shimazaki and Nakata, 1980; Youngs and Coppersmith, 1985). However, paleoseismic and instrumental records indicate considerable deviation from these end-members (Weldon et al., 2004; Chen et al., 2020), highlighting the inherent complexity of the faulting process.

The space-time recurrence pattern of earthquakes is documented at major plate boundaries worldwide along continental transform faults (Sieh and Jahns, 1984; Weldon et al., 2004; Rockwell et al., 2015; Scharer and Yule, 2020; Agnon, 2014; Marco and Klinger, 2014; Ran et al., 2019), continental collisions (Sapkota et al., 2013; Bollinger et al., 2013), and subduction zones (Moernaut et al., 2018; Sawai, 2020; Goldfinger et al., 2003; Nelson et al., 2006; Patton et al., 2015; Rubin et al., 2017). The paleoseismic record indicates substantial variations of the time intervals and the spatial distributions of coseismic slip of consecutive events (Sieh, 1996; Sykes and Menke, 2006). Although some faults rupture fairly regularly (Berryman et al., 2012) and others seem to produce characteristic coseismic slip distributions (Klinger et al., 2011), a majority of faults exhibit more temporal clustering and more dissimilar slip distributions. For example, seismic super-cycles showcase smaller-magnitude earthquakes between much larger events (Sieh et al., 2008; Goldfinger et al., 2013; Philibosian et al., 2017; Usami et al., 2018; Nocquet et al., 2017; Philibosian and Meltzner, 2020; Barbot, 2020).

While increasingly well documented, the physical mechanisms underpinning the spatial and temporal variability of the seismic cycle remain poorly understood, but there is more. Seismicity embodies a wide range of rupture styles varying from slow-slip events and tremors to slow earthquakes and fast ruptures (Peng and Gomberg, 2010; Obara and Kato, 2016; Nishikawa et al., 2019).

* Corresponding author.
*E-mail address:* shiyingn@usc.edu (S. Nie).

https://doi.org/10.1016/j.epsl.2022.117593
0012-821X/

Large earthquakes exhibit much diversity, with unilateral and bilateral rupture propagation (Ross et al., 2020), crack-like ruptures and self-healing sustained, decaying, or growing pulses (Heaton, 1990; Wang and Day, 2017), and sub-Rayleigh and super-shear ruptures (Dunham and Archuleta, 2004; Bao et al., 2019). Although fundamentally linked by fault mechanics, the relation between recurrence patterns and rupture styles is poorly understood. Here, we use numerical simulations that consistently resolve all phases of the seismic cycles in space and time to describe the possible connection between rupture styles and recurrence histories assuming a simple structural setting with a single fault embedded in a compliant fault zone.

The control of frictional properties on the rupture style in a homogeneous medium is well documented (e.g., Lapusta and Rice, 2003; Wu and Chen, 2014; Kato, 2014; Veedu and Barbot, 2016; Barbot, 2019b; Nie and Barbot, 2021), but the surrounding compliant zone may have a strong influence on rupture propagation, peak slip velocity, ground motion (Harris and Day, 1997; Duan, 2008; Huang and Ampuero, 2011), and on the emergence of pulse-like ruptures (Kaneko et al., 2011; Abdelmeguid et al., 2019; Idini and Ampuero, 2020; Thakur et al., 2020). Compliant zones develop from the successive damage accumulation during seismic ruptures that causes measurable elastic moduli reduction (Fialko et al., 2002; Barbot et al., 2008, 2009). A combination of petrologic, seismological, and geodetic studies indicate a wide range of compliance and fault zone thickness (e.g. Chester and Logan, 1986; Chester et al., 1993; Li et al., 1994; Vidale and Li, 2003; McGuire and Ben-Zion, 2005; Chen and Freymueller, 2002; Fialko, 2004; Hamiel and Fialko, 2007b; Cochran et al., 2009; Shapiro et al., 2005). The effect of a compliant fault zone within the quasi-dynamic or quasi-static approximations has been documented for one or more physical parameters within a limited range. The goal of this study is to jointly explore the recurrence patterns, slip distributions, and source characteristics of the ruptures that consistently unfold for a wider range of attributes of the compliant zone and frictional properties of the fault interface.

The content of this manuscript is arranged as follows. In Section 2, we describe the physical assumptions and the numerical model setup. In Section 3, we characterize the rupture styles, from creep and slow-slip events to complex pulse-like rupture sequences, and their associated recurrence patterns in the parametric space of the characteristic weakening distance and the fault zone rigidity. In Section 4, we explore the effect of the fault zone properties on rupture cycles. Our simulations indicate a wide range of recurrence patterns, from single- to multiple-periodic, to apparently chaotic, culminating with mainshock-aftershock sequences, with ruptures going from characteristic to more dissimilar. These variations seem to go hand in hand with specific rupture styles, from crack-like to pulse-like ruptures, associated with a specific range of structural and frictional properties that can be described by a single non-dimensional parameter representative of the velocity-weakening region and its surrounding compliant zone.

## 2. Physical assumptions and methods

Our goal is to determine the possible relationship between the style and recurrence pattern of ruptures that emerge spontaneously in seismic cycles under the rate- and state-dependent frictional framework (Dieterich, 1979; Ruina, 1983; Rice and Ruina, 1983). We consider a simplified mechanical system consisting of a single fault embedded in a compliant zone as a numerical analog for the seismogenic zone. We ignore the viscoplastic deformation of the compliant zone (Mia et al., 2022; Erickson et al., 2017) and the resulting incremental damage accumulation during each seismic rupture (Lyakhovsky et al., 2001). We assume that the evolution of fault slip is controlled by the frictional resistance along the fault plane and that all aspects of fault dynamics are determined by the combination of frictional, physical, and structural properties of the system. We consider a two-dimensional approximation in condition of anti-plane strain relevant to long strike-slip faults. While the two-dimensional approximation is sufficient to capture many ruptures styles and recurrence patterns, some important end-members, such as period-multiplying cycles of both slow and fast ruptures, only occur in three-dimensional models. For example, successive slow and fast rupture cycles emerge near the stability transition in finite faults due to coexisting mode II and mode III ruptures, which have slightly differing stability conditions (Veedu and Barbot, 2016; Barbot, 2019b; Veedu et al., 2020).

We use the multiplicative form of the rate- and state-dependent friction law without thermal effects. The friction law can be derived from first principles assuming that the real area of contact density formed at contact junctions follows (Barbot, 2019a)

$$\mathcal{A} = \frac{\mu_0 \bar{\sigma}}{\chi} \left( \frac{\theta V_0}{L} \right)^{\frac{b}{\mu_0}} \tag{1}$$

where $\mu_0$ is the reference friction coefficient at reference sliding velocity $V_0$, $\bar{\sigma}$ is the effective normal stress including the Terzaghi pore-pressure effect, and $\chi$ is the indentation hardness of the surface. In addition to a linear dependence on effective normal stress, the real area of contact density is modulated by a state variable $\theta$ representing the age of contact with the reference age $L/V_0$ and the power exponent $b \ll 1$, allowing contact growth during locked periods and contact erosion at finite sliding velocity. In isothermal condition, the sliding velocity follows the power-law constitutive relationship (Barbot, 2019a)

$$V = V_0 \left( \frac{\tau}{\chi \mathcal{A}} \right)^{\frac{\mu_0}{a}} , \tag{2}$$

where $V$ is the local sliding velocity, the product $\chi \mathcal{A}$ represents a time- and state-dependent yield strength, and $a \ll 1$ is a power exponent. Inverting the relationship, we obtain the multiplicative form of rate- and state-dependent friction

$$\tau = \mu_0 \bar{\sigma} \left( \frac{V}{V_0} \right)^{\frac{a}{\mu_0}} \left( \frac{\theta V_0}{L} \right)^{\frac{b}{\mu_0}} \tag{3}$$

independent of the indentation hardness of the material, explaining why hard and soft rocks have the same coefficient of friction (Byerlee, 1978). As the logarithmic form of rate- and state-friction represents the linear terms of the Taylor series expansion of the multiplicative form, similar behaviors are expected under common conditions. However, the multiplicative form supersedes the logarithmic form for vanishing velocity and truly stationary contact. Further, we assume that contact aging and erosion follow the aging law in isothermal conditions (Ruina, 1983)

$$\dot{\theta} = 1 - \frac{V\theta}{L} , \tag{4}$$

allowing healing at truly stationary contact. The aging law captures the time-dependent flattening and rejuvenation of contact junctions that form the real area of contact at the fault interface with the characteristic slip distance $L$. The fault is situated along the center of a compliant zone with a uniform thickness $T$ and rigidity $G_{cz}$, potentially differing from the country rocks with rigidity $G$ in the surrounding two half-spaces. The resulting computational domain is a full space — without a free surface — centered on the compliant fault zone (Fig. 1).

To investigate a wide range of fault zone and frictional properties efficiently, we use the spectral boundary-integral method.

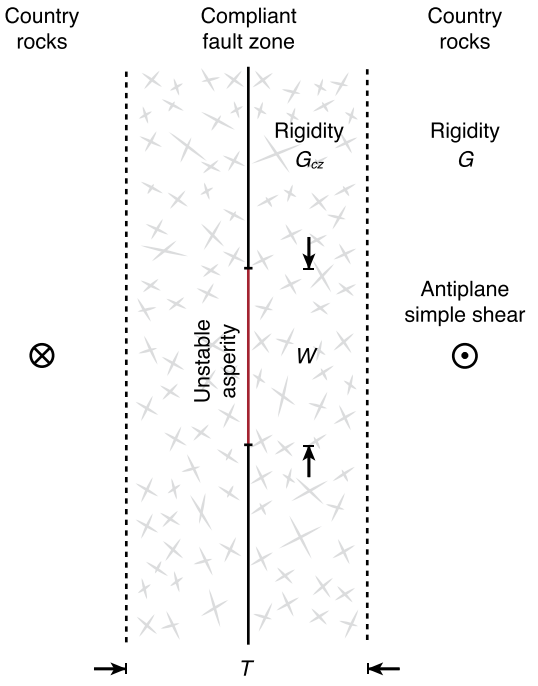


**Fig. 1.** Schematic representation of the simplified compliant fault zone model. The rigidity of the bedrock and the fault zone are $G$ and $G_{cz}$, respectively. The fault zone thickness is $T$. The central unstable patch of width $W$ is surrounded by a velocity-strengthening fault.

We simulate quasi-dynamic seismic cycles within a whole space with the radiation damping approximation. The Green's functions of stress interactions are derived in the frequency domain and the numerical efficiency is obtained with the fast Fourier transform, fifth-order accurate adaptive time steps, and shared memory parallelism (Barbot, 2021). To incorporate the compliant zone surrounding the fault, we use the corresponding stress interaction kernel, which has a closed-form expression in the Fourier domain (Idini and Ampuero, 2020). For all the models considered, the effective normal traction is $\bar{\sigma} = 100$ MPa, the reference coefficient is $\mu_0 = 0.6$, and the reference velocity is $V_0 = 10^{-6}$ m/s. The power exponent for the velocity dependence is uniform along the fault with $a = 10^{-2}$. The long-term loading rate that drives the seismic cycle is $V_{\mathrm{L}} = 10^{-9}$ m/s or about 32 mm/yr. To represent the seismogenic zone, we consider a single velocity-weakening area surrounded by a velocity-strengthening region. The fault extends from -8.2 to 8.2 km and the velocity-weakening region spreads from -2.5 to 2.5 km from the origin at the center of the computational domain. The power exponent for the state-dependence is piece-wise homogeneous, with $b = 1.4 \times 10^{-2}$ in the central velocity-weakening area and $b = 0.6 \times 10^{-2}$ in the surrounding region. We consider the quasi-static process zone $\Lambda_0$ at the rupture speed $0^+$, which describes the area near the rupture front during the breakdown of the fault resistance, as the critical length scale in the system (Day et al., 2005)

$$\Lambda_0 = \frac{G_{cz} L}{b\bar{\sigma}} \,. \tag{5}$$

The finest models hold $2^{15}$ surface elements of 50 cm width. For all the models presented herein, the grids are finer than $\Lambda_0/4$, which we found sufficient to attain numerical convergence.

Within our physical assumptions, the rupture style and recurrence pattern are controlled by a small set of independent non-dimensional parameters (Appendix A). The Dieterich-Ruina-Rice number

$$R_u = \frac{W}{h^*} \tag{6}$$

corresponds to the ratio of the asperity size $W$ to a characteristic nucleation size $h^*$ that depends on the rigidity structure and controls the dynamics of ruptures. The $R_b$ number

$$R_b = \frac{b-a}{b} \tag{7}$$

controls the state evolutionary effects and the emergence of complex slow-slip events. The range of rupture styles that spontaneously emerge as a function of these parameters in a homogeneous crust is well understood (Wu and Chen, 2014; Barbot, 2019b; Nie and Barbot, 2021). However, the presence of a compliant zone introduces two other non-dimensional parameters, namely the ratio of country-rock to fault zone rigidity $G/G_{cz}$ and the width of the compliant zone relative to the seismogenic zone $T/W$. A key question that has long animated the community is whether a compliant zone generates unique rupture styles and recurrence patterns that cannot take place in the simpler structural setting of a homogeneous medium (Huang and Ampuero, 2011; Huang et al., 2014; Pelties et al., 2015; Huang, 2018; Abdelmeguid et al., 2019; Idini and Ampuero, 2020; Thakur et al., 2020). To address this question for quasi-dynamic seismic cycles simulations, we explore a range of characteristic weakening distance, compliance ratio, and fault zone thickness compatible with laboratory and field observations of fault zones.

## 3. Rupture styles and recurrence patterns

We examine the rupture styles and recurrence patterns that spontaneously evolve in numerical models of the seismic cycle under the rate- and state-dependent friction framework in the presence of a pre-existing compliant zone. We explore a wide range of characteristic weakening distance from 0.5 to 125 mm covering representative values inferred from the laboratory (Marone and Kilgore, 1993; Mei et al., 2021, 2022) and geophysical observations (Ellsworth and Beroza, 1995; Fukuyama and Mikumo, 2007) within the practical constraints of numerical calculations. Varying the characteristic weakening distance is an efficient way to control the rupture styles, from slow-slip events to fast earthquakes. We consider a fixed ratio of power exponents $a$ and $b$ because varying the $R_b$ number is only critical to control the seismogenic potential of slow-slip events (Nie and Barbot, 2021), which is not the focus of the current study. Additionally, we explore a wide range of compliance levels from homogeneous with the country rocks to a factor of five of rigidity reduction within the fault zone, compatible with seismo-geodetic observations for various faults (Fialko et al., 2002; Hamiel and Fialko, 2007a; Barbot et al., 2009; Cochran et al., 2009). In a preliminary step, we consider a fixed compliant zone thickness of 2 km. This forms a wide two-dimensional parameter space documenting the effects of frictional and structural properties of fault zones. We explore the effect of the thickness of compliant zones in the next section. We sample the characteristic weakening distance with 25 values nearly uniformly distributed in logarithmic space. For each case, we explore 21 compliance levels, uniformly distributed between $G/G_{cz} = 1$ to 5. The resulting 525 simulations document the evolution of possible rupture style and recurrence patterns in the two-dimensional space of structural and frictional parameters. The simulations run for up to $10^7$ iterations, but the simulated time varies from less than a year to thousands of years, depending on the parameters.

The simulations feature seismic cycles with distinct rupture styles including steady sliding, waves of partial coupling, periodic slow-slip events, bilateral and unilateral ruptures, crack-like ruptures with aftershock and foreshock sequences, and chaotic cycles

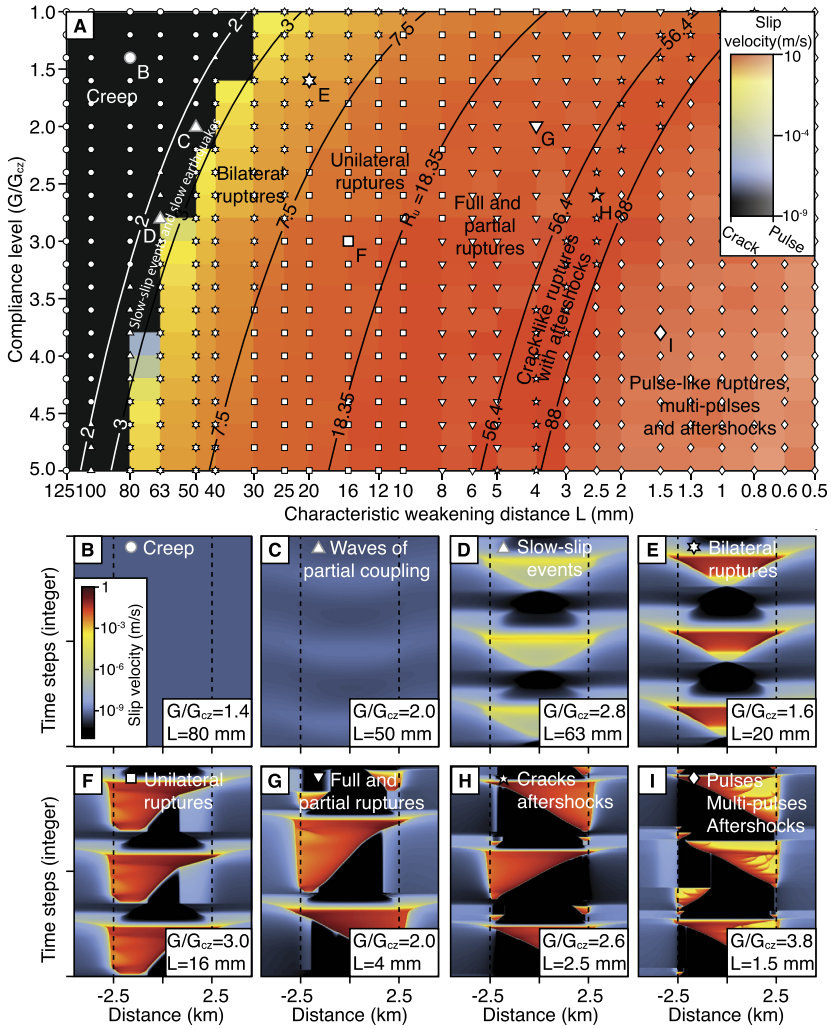


**Fig. 2.** Seismic cycle simulations under variable characteristic weakening distance and fault zone compliance level. a) Sub-domains for creep, slow slip, bilateral and unilateral periodic ruptures, crack-like ruptures and pulse-like ruptures. Contours are the $R_u$ numbers of the models. The symbols represent the rupture styles of the models used to produce this phase diagram. The background color indicates the peak slip velocity and the shading represents the crack-like to pulse-like rupture transition. b to i) Examples of different rupture styles, represented by the slip velocity. The x- and y-axes represent down-dip distance on the fault and time steps, respectively. The area between dash lines is the velocity-weakening domain. (For interpretation of the colors in the figure(s), the reader is referred to the web version of this article.)

of pulse-like ruptures (Figs. 2 and S1). Each style of seismic cycle occurs within a well delineated range of compliance level and characteristic weakening distance. The transition from any rupture style to another can be obtained by varying either the characteristic weakening distance or the compliance level. At first order, the domain boundaries of all distinct rupture styles can be predicted by contours of constant Dieterich-Ruina-Rice number if the characteristic nucleation size incorporates the effect of elastic layering. As the effective rigidity near the fault zone depends on the wavelength of fault slip, the estimate of nucleation size solves the transcendental equation (Appendix B) (Kaneko et al., 2011; Idini and Ampuero, 2020)

$$\frac{1}{R_u}\tanh\left[\lambda\frac{T}{W}R_u+\operatorname{arctanh}\frac{G_{cz}}{G}\right]=\frac{G_{cz}}{(b-a)\bar{\sigma}}\frac{L}{W}\,, \tag{8}$$

where the coefficient $\lambda=\pi/4$ is introduced for the anti-plane setting (Kaneko et al., 2011) and to fit the observed boundaries of rupture styles in our simulations. The solution to Equation (8) provides a smooth transition between the two end-member cases whereby either the fault zone or country rock rigidity fully controls the elastic interactions, in which case the domain is effectively homogeneous. The transitions from creep to waves of partial coupling, to slow-slip events, to bilateral ruptures and unilateral ruptures, to crack-like and pulse-like ruptures with aftershock sequences occur at $R_u=2$, 3, 7, 18, 56, and 88, respectively. In all of our simulations, we do not observe any rupture style or recurrence pattern with a compliant zone that does not also emerge in a homogeneous medium with a smaller characteristic weakening distance.

The exploration of a vast parameter space shows that the transition from crack-like to pulse-like rupture propagation is promoted by increasingly compliant fault zones, consistent with previous findings (Huang and Ampuero, 2011; Pelties et al., 2015), but also by a smaller characteristic weakening distance (Fig. 3). We examine every rupture in the simulations to determine the rupture style, looking to identify growing, steady, and decaying pulse-like, as well as crack-like rupture propagation by visual inspection. Additionally, we calculate the ratio of fast rupture area (velocity larger than $10^{-2}$ m/s) over the total rupture area in space and time as a proxy of pulse-like or crack-like modes. The average among all events is used as a representative value for the phase diagram in Fig. 3a. For a relatively large characteristic weakening distance or a mild rigidity contrast, the ruptures propagate like cracks, e.g., the case in Fig. 3b for $L=2$ mm and $G/G_{cz}=2$. The rupture stops when it reaches the velocity-strengthening area

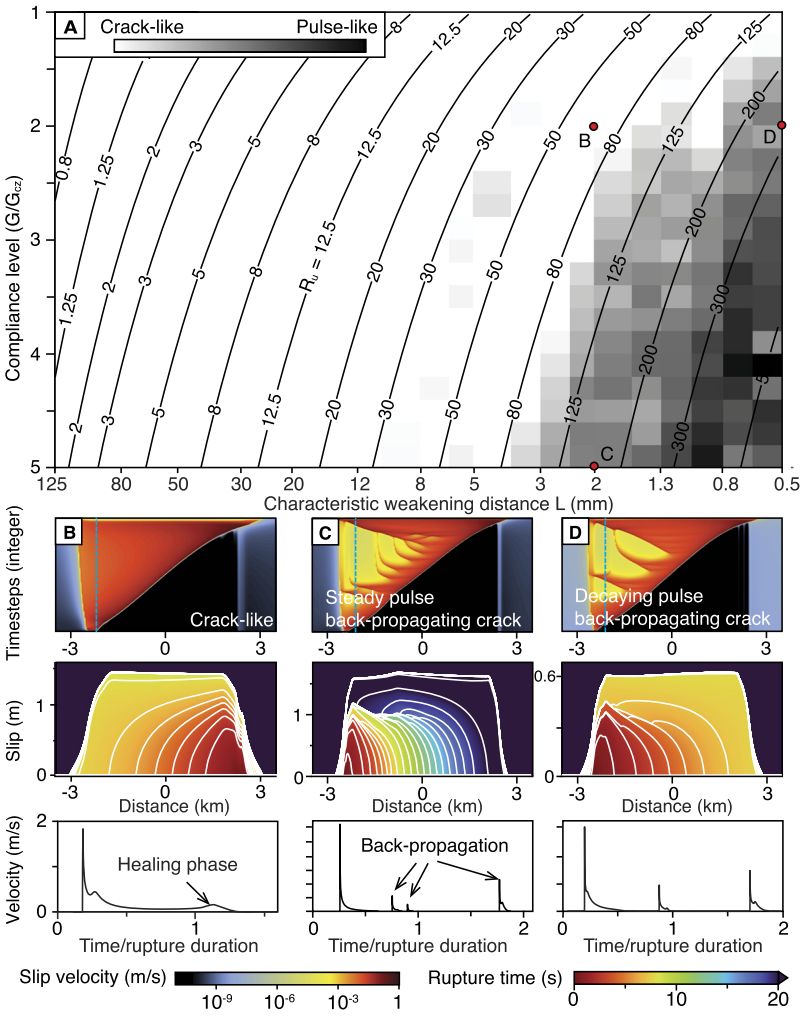


**Fig. 3.** Crack-like to pulse-like rupture transitions under variable characteristic weakening distance and compliance level of the fault zone. a) The proportion of crack-like versus pulse-like rupture style. Contours are for constant $R_u$ numbers. b) A typical crack-like rupture propagation for a simulation with $G/G_{cz} = 2$ and $L = 2$. The upper panel is the slip velocity versus time steps; the middle panel shows the rupture history with 1-second interval contour; the lower panel is the source time function with the sampling locations shown as the blue line in upper panel, close to the hypocenter. c) and d) pulse-like rupture models differing from b) by increasing the compliance level or reducing the characteristic weakening distance, respectively.

and the rise time is commensurate with the rupture time. The simulated events with either a lower fault zone rigidity, e.g., the case in Fig. 3c for $L = 2$ mm and $G/G_{cz} = 5$, or shorter characteristic slip weakening distance, e.g., case in Fig. 3d with $L = 0.5$ mm and $G/G_{cz} = 2$, tend to propagate like a pulse albeit with multiple sub-events and back-propagating rupture fronts. The source-time functions include several peaks, leading to a less reliable rise-time determination. Despite the crack-like back-propagation at the end of the rupture, a rise time of about 20% of the rupture duration for a point located near the hypocenter makes it a firmly pulse-like rupture. Among all the simulations considered, some ruptures exhibit steady pulse-like propagation, e.g., Fig. 3c. Other simulations produce decaying pulses, e.g., Fig. 3d, but we could not identify any growing pulses. The transition from crack-like to pulse-like ruptures occurs gradually for $R_u$ numbers between about 85 and 100.

The sequences with distinct rupture styles show different temporal and spatial recurrence patterns (Fig. 4 and 5). Following a common practice in paleoseismic studies, we describe the variability of temporal recurrence patterns with the coefficient of variation (CoV), i.e., the standard deviation divided by the average recurrence time. We use the proportion of the number of full ruptures over total number of events to describe the spatial recurrence behavior. The bilateral-rupture family exhibits periodic sequences with minimum coefficient of variation (Fig. 4b) and purely characteristic ruptures (Fig. 5b). The cycle of unilateral full and partial ruptures showcase another periodic recurrence pattern including two major and two minor events within one cycle (Fig. 4c and Fig. 5c), which we refer to as periodic-n sequences, here with $n = 4$. Both periodic and periodic-4 sequences are considered time- and slip-predictable based on their slip deficit evolution (right panels of Fig. 4b and 4c). The recurrence pattern becomes less regular for larger $R_u$ number for which aftershock sequences occur (panels d and e in Fig. 4 and 5). The crack-like sequences can still be considered quasi-periodic, having a CoV less than 1 and 75% of the earthquakes rupturing a similar area. For even larger $R_u$ numbers, the pulse-like ruptures occur more randomly, associated with a high CoV and less characteristic ruptures. The complex recurrence patterns of the cycles at high $R_u$ number are manifested by their slip-deficit history that falls neither in the slip-predictable nor time-predictable end-members (right panels of Fig. 4d and e), and the cycle of pulse-like ruptures exhibiting apparently larger deviations. For $R_u > 125$, the period separating consecutive full ruptures is a super-cycle that includes multiple smaller ruptures. The CoV cannot be used to differentiate all the cases in our simulations. For instance, the periodic-n cycles display a high CoV and low proportion of full-ruptures (Figs. 4a and 5a) because the large

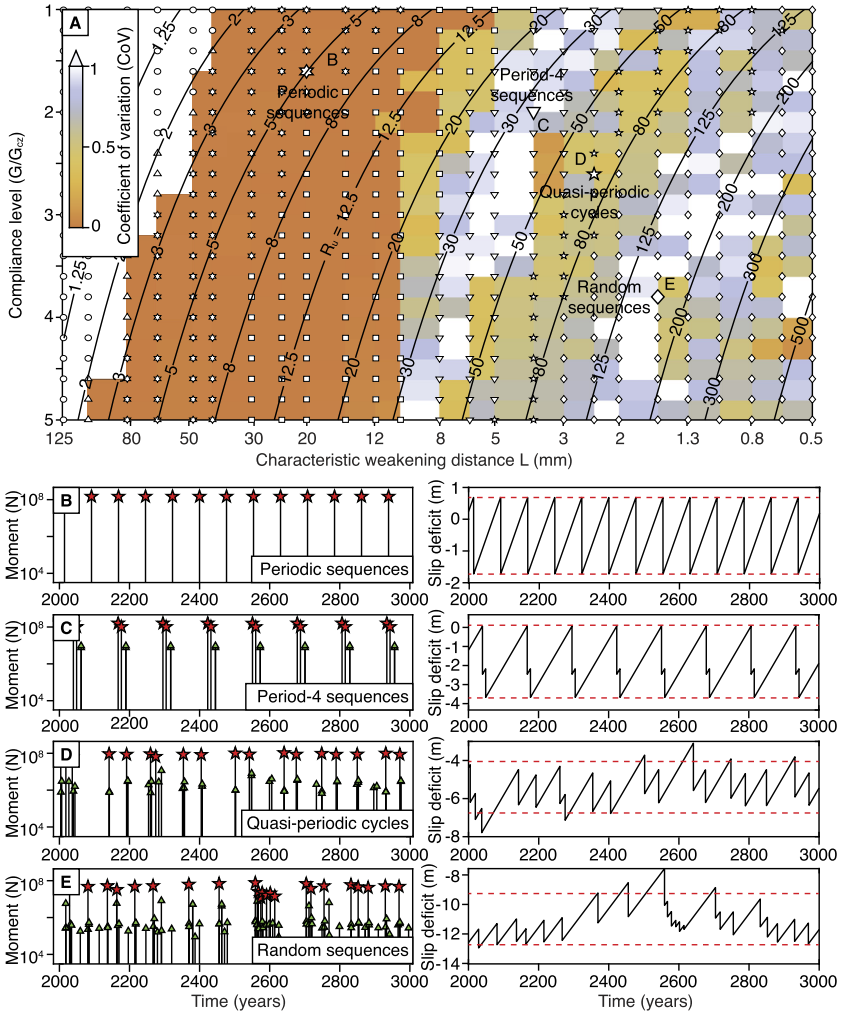


**Fig. 4.** The relationship between rupture styles and temporal recurrence patterns. a) Phase diagram of coefficient of variation (CoV, standard deviation divided by mean of the recurrence time of major earthquakes) of the major events (events that rupture at least half of the fault). The contours are the $R_u$ numbers of the models. b) to e) The left plots show the earthquake timelines and moments for four parametric regimes labeled in a). The stars indicate the major events used to calculate the CoV in a), while the triangles indicate the minor events. The right plots show the corresponding slip deficit. The upper and lower dash lines in each figure show the approximated limit of the slip- and time- predictable models, respectively.

earthquakes are systematically followed by two partial ruptures, reducing the mean and enlarging the standard deviation of the recurrence intervals. The pulse-like sequences at high $R_u$ numbers have variable CoV and proportion of full ruptures, primarily due to fewer simulated events in each simulation due to numerical limitation, but the recurrence behavior of these models is visibly complicated.

As the cycles increase in complexity with a transition from crack-like to pulse-like ruptures with a lower proportion of full ruptures, aftershocks also appear at higher $R_u$ numbers (Fig. 6). For this analysis, an aftershock is defined as an earthquake that happens during the postseismic phase of a mainshock, characterized by fast afterslip in the velocity-strengthening region. In our simulations, we define a mainshock as an event that ruptures more than half of the velocity-weakening patch. We determine the end of a postseismic period when the peak slip rate drops below a threshold of twice the background loading rate or another mainshock occurs. The number of aftershocks increases for more compliant fault zones and for smaller characteristic weakening distance, which can be captured by boundaries of constant $R_u$ numbers. The aftershocks start to occur for $R_u > 30$, but only one aftershock occurs per rupture tip for $30 < R_u < 150$ (Fig. 6c and d). For the models with $R_u$ between 150 to 400, 2 aftershocks occur for each rupture tip, resulting in an average amount of 4 aftershocks per mainshock (Fig. 6e and f). The number of aftershocks can be more than 10 for extremely large $R_u$ cases, which occurs during nested aftershock sequences — when large aftershocks trigger their own aftershock sequence. We use the sequences with at least two aftershocks at each rupture tip to analyze the time-dependent seismicity rate, and we treat the aftershocks at the top and bottom of the seismogenic zone separately (Fig. 6i). The seismicity rate is calculated as the reciprocal of the time gap between two subsequent aftershocks. The seismicity rate decays following approximately $t^{-1}$ with some scatter associated with nested aftershock sequences.

The rate of natural aftershocks follows the Omori-Utsu law (Omori, 1894; Utsu, 1961)

$$\dot{N}(t) = \frac{K}{(c+t)^p}\ , \tag{9}$$

where $K$, $c$ and $p$ are site-dependent constants and $t$ is the time since the mainshock. Our aftershock dataset can be explained by $\dot{N}(t) = 1/t$, which conforms to the Omori law with $K = 1$, $p = 1$ and $c = 0$. In our models, the aftershocks occur in the velocity-weakening region as a result of a temporary acceleration of the local loading rate that accompanies afterslip in the nearby velocity-

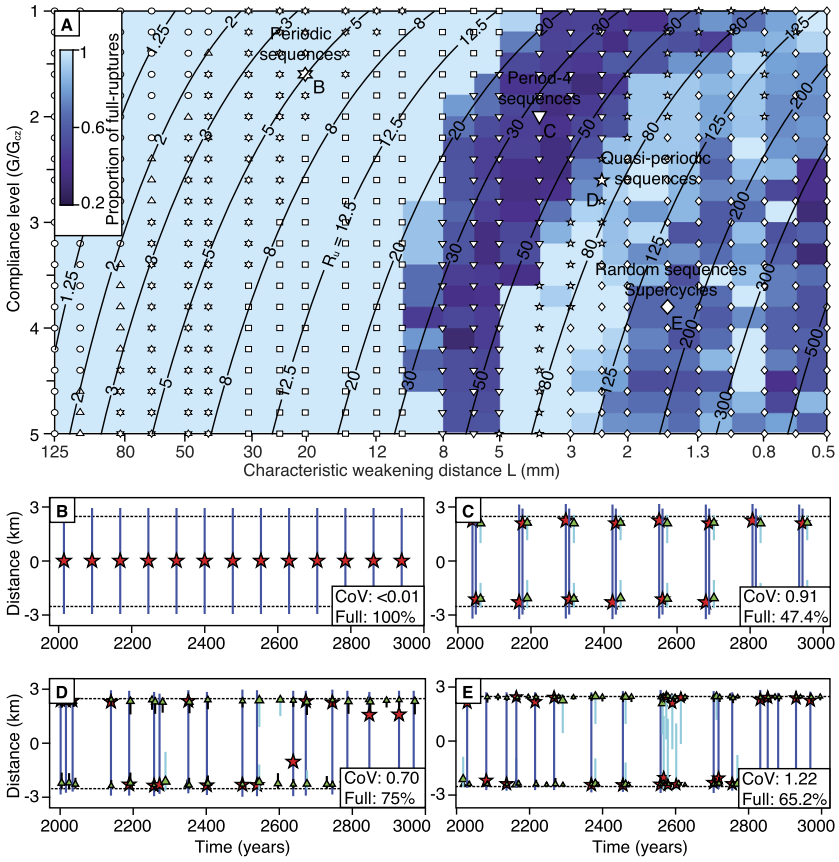


**Fig. 5.** Relationship between rupture styles and spatial recurrence patterns. a) Phase diagram of proportion of full-ruptures, excluding the events that rupture less than 20% of the seismogenic zone. The threshold for a full rupture is 90% of the seismogenic zone. The contours are the $R_u$ numbers of the models. b) to e) The rupture area of the earthquakes from four parametric regimes labeled in a). The stars indicate the hypocenters of major events used to calculate CoV, while the triangles indicate the hypocenter of minor events. The dark blue lines represent rupture areas of full ruptures mentioned in b). The light blue lines are counted as partial ruptures. The black ones are ignored for this analysis.

strengthening region. As afterslip decays as 1/t (Montési, 2004), it drives the aftershock sequence with a similar decay rate (Perfettini and Avouac, 2004). The value of $p$ and $c$ of our models is in the observational range. However, the productivity parameter $K$ is much smaller than in nature due to the limited structural and rheological complexity in the model.

Our findings suggest that the spatial and temporal recurrence behaviors are controlled by the $R_u$ number of the fault zone. At high $R_u$ number, the characteristic nucleation size is small enough that partial ruptures develop near the boundaries of the velocity-weakening region, where the loading rate is higher. These partial ruptures delay the wall-to-wall ruptures and leave behind stress concentrations within the velocity-weakening region that affects the rupture propagation of subsequent events. These two effects contribute to the breakdown of the time-predicable model. Furthermore, partial ruptures produce different slip from the full ruptures despite a similar stress drop, due to the variation of the rupture length. This effect breaks down the slip-predictable model. As a result, the seismic cycle at high Ru number follows neither the time- nor the slip-predictable models. Our results also suggest that the change of recurrence behavior is deeply linked to associated changes in rupture styles. Models with high $R_u$ numbers tend to feature complex recurrence patterns in time and space, manifesting as pulse-like events with random recurrence patterns, culminating in mainshock-aftershock sequences. In contrast, the low $R_u$ cases are relatively simple, with crack-like ruptures and more periodically occurring large events.

## 4. The effect of compliant fault zones

In this study, we explore the frictional and compliant zone properties to disentangle their respective effects. The Dieterich-Ruina-Rice number provides a good estimate of the boundaries of the parameter domains producing similar rupture styles. This is highlighted by laying out the rupture characteristics found in the previous section (Fig. 2) based on the corresponding $R_u$ number instead of the physical units used. With a few exceptions, the rupture styles are associated with a clear range of $R_u$ numbers (Fig. 7a). In order to draw a more complete picture of the impact of fault zone structure on seismic cycles, we explore additional models with a compliant zone thickness ranging from 20 meters to 200 kilometers with the characteristic weakening distance ranging from 0.6 mm to 63 mm, and the fault zone rigidity contrast also increasing from 1.2 to 4.6 (Fig. S2). Without exception, the boundaries between different rupture styles still occur at fixed $R_u$ number (Fig. 7b).

For the purpose of predicting rupture styles and recurrence patterns, the parameter space can be reduced from the three-dimensional parameter volume of $L$, $G_{cz}$, and $T$ to a one-dimensional line of varying $R_u$ numbers. This is further confirmed by comparing simulations for varying compliance, thickness, and characteristic weakening distance with a similar $R_u$ number for the cases of $R_u = 5.33$, 11, 28.5, 98 (Fig. 8). The sequences with similar $R_u$ show a similar behavior. The simulations for varied fault zone thickness combined with insights from the definition of Equation (8) of the $R_u$ number indicate that the effect of a finite fault zone thickness is of consequence only within a narrow range

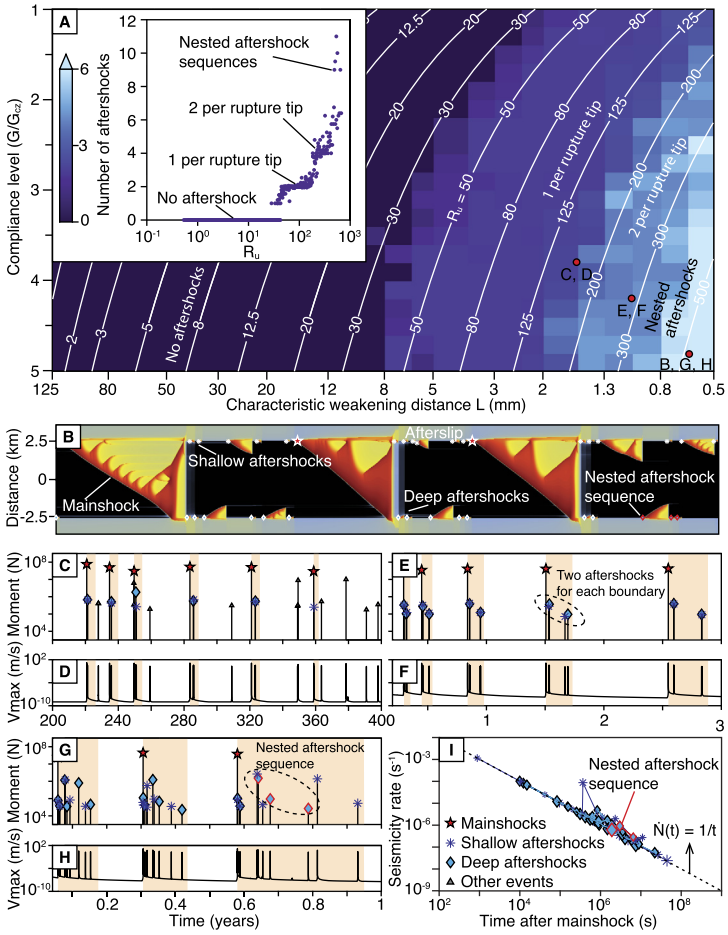


**Fig. 6.** The statistics of aftershocks under variable characteristic weakening distance and compliance level of the fault zone. a) Number of aftershocks per mainshock. The contour lines are the $R_u$ number of the simulations. The inset shows the number of aftershock as a function of $R_u$ for all the 525 simulations. b) Velocity vs time step and terminology, the parameters are shown on a). c), e), and g) display the time history and moment of the mainshocks and aftershock sequences. The shaded areas are the postseismic periods. d), f), and h) is the corresponding peak slip velocity used to define the postseismic period. i) Seismicity rate of aftershocks as a function of time from the mainshock. In all of b-i), the stars represent the mainshocks. The asterisk and diamonds represent shallow and deep aftershocks, respectively. The triangles are the remaining events.

(Fig. 8). A fault zone thickness $T > 2h^*$, with $h^* = W/R_u$, is large enough to form an effectively uniform domain and its rigidity controls the characteristic nucleation size. Similarly, if the thickness is smaller than this threshold by an order of magnitude or more, the fault dynamics is controlled by the rigidity of the country rocks.

The rupture behaviors documented in previous studies can be obtained for various combinations of frictional and structural parameters or any change of $R_u$ number (Figs. 2 and 7). For example, for the large characteristic weakening distance regime of $L = 5$ cm, increasing the compliance level brings the behavior from creep, to slow-slip events, and ultimately to earthquakes, thus increasing the peak slip velocity significantly. In a moderate characteristic weakening distance regime, such as for $L = 16$ mm, the ruptures transition from bilateral to unilateral, resulting in the alternation of hypocenter locations. The cases with small characteristic weakening distance, e.g., $L = 1$ mm, show a transition from crack-like to pulse-like rupture propagation, with the apparition of back-propagating rupture sub-fronts. At first order, these phenomena are mainly associated with varying the $R_u$ number, and can be achieved by either modifying the characteristic weakening distance or other fault zone properties.

## 5. Discussion

In this study, we describe the quasi-dynamics of a two-dimensional planar fault embedded in a compliant zone. The numerical simulations document the link between the rupture styles and the recurrence patterns of major earthquakes. The rupture styles range from slow-slip events, waves of partial coupling, unilateral and bilateral ruptures, full and partial ruptures, culminating with mainshock-aftershock sequences with either crack-like or pulse-like rupture propagation. The recurrence patterns for bilateral and unilateral ruptures follow the slip- and time-predictable models. For increasingly unstable faults, as the sequence changes from strictly periodic to multiple periodic, i.e., a repeating sequence that involves multiple events, aftershocks emerge. In the parameter regime that produces more pulse-like ruptures and an increasing amount of aftershocks, the slip evolution deviates wildly from the slip- or time-predictable models. The variability of recurrence time is fundamentally linked to the emergence of partial ruptures. The models with the most unstable faults produce coefficients of variation greater than unity, a telltale sign of deterministic chaos.

The strong relationship between rupture style and recurrence patterns may shed new light on paleoseismic records. For example, the occurrence of characteristic ruptures at the Fuyun Fault in China (Klinger et al., 2011) suggests a large characteristic nucleation size, which is associated with crack-like rupture propagation in our models. The otherwise scarcity of characteristic ruptures implies that most active faults have a small characteristic nucleation size compared to their seismogenic length, which also im-

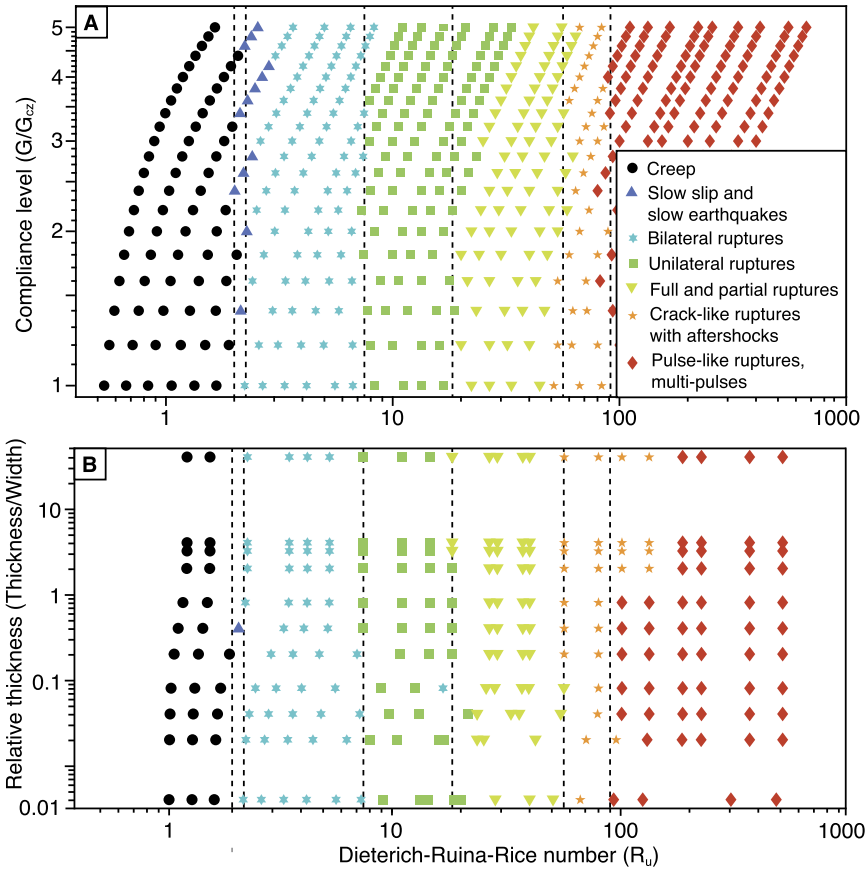


**Fig. 7.** Efficiency of the $R_u$ number to describe the rupture style. a) Rupture style for varying compliance level and characteristic weakening distance for a fixed compliant zone thickness of $T = 2,000$ m. b) Rupture style for varying fault zone thickness, characteristic weakening distance, and compliance ratio $G/G_{cz}$. The corresponding parameters are in the supplement. The dash lines are the approximation of $R_u$ thresholds of rupture styles.

plies recurrence patterns that tend to deviate from slip- and time-predictable models. A well-documented example is at Wrightwood, California (Weldon et al., 2004), where the evolution of fault slip shows a substantial deviation from the time- and slip-predictable models, compatible with a parameter regime leading to a high Dieterich-Ruina-Rice number. This implies that the Mojave section of the San Andreas Fault is greatly unstable, its along-strike length being much greater than the characteristic nucleation size of earthquakes. This can be accomplished by a substantial reduction of rigidity in the surrounding compliant zone and/or a small characteristic weakening distance. Even though our geometrically simple model can produce complex recurrence patterns that deviate from time- and slip-predictable behavior, other aspects may also contribute in nature, such as geometrical and frictional heterogeneity.

The chaotic sequence of full and partial ruptures may explain the so-called seismic super-cycles observed at the Sumatra (Sieh et al., 2008; Philibosian et al., 2017; Philibosian and Meltzner, 2020), Northeast Japan (Usami et al., 2018), Ecuador (Nocquet et al., 2017) and Cascadia (Goldfinger et al., 2013) subduction zones. The model implies a strong deviation from the time- and slip-predictable models during super-cycles, as observed (Sieh et al., 2008), presumably caused by numerous smaller ruptures, aftershocks and creep within the velocity-weakening region that redistribute stress and yet cannot be detected in the geologic record. The succession of several partial ruptures before a through-going rupture is a hallmark of super-cycles, explaining why the short paleoseismic records at the Japan trench was insufficient to herald an imminent giant earthquake (Barbot, 2020). This behavior is, in fact, the natural response of even a simple model with only a single unstable patch. As seismic super-cycles seem common at subduction zones, it implies that subduction megathrusts have a small characteristic nucleation size compared to the down-dip width of the seismogenic zone.

Understanding the rupture propagation style of earthquakes has important implications on the radiated energy and ground motion (Lambert et al., 2021). Some finite-fault inversions suggest that large earthquakes are preferentially pulse-like (Heaton, 1990). Several mechanics have been proposed to explain pulse-like ruptures, such as strong weakening during flash heating and thermal pressurization (Wang and Day, 2017; Lambert et al., 2021), heterogeneity of stress (Beroza and Mikumo, 1996), and specific geometry of the seismogenic zone (Day, 1982; Wang et al., 2019). Our results corroborate others based on a quasi-dynamic approach (Barbot, 2019b; Idini and Ampuero, 2020) and suggest that a large $R_u$ number, whether due to the presence of a compliant fault zone or any other relevant physical characteristics, can also yield pulse-like ruptures. In this parameter regime, stress heterogeneities spontaneously develop as multiple partial ruptures leave behind residual stress concentration at the rupture tip. This heterogeneous initial stress at the onset of ruptures creates the condition for a pulse-like rupture propagation. In our models, pulse-like ruptures occur in the regime that also produces complex recurrence patterns, non-characteristic slip distributions, and substantial deviation from the time- and slip-predictable models.

Our results also help characterize a physical range for the coefficient of variation in paleoseismic records. For example, the longest continuous record of paleo-earthquakes at Hokuri Creek in the Alpine Fault, New Zealand (Berryman et al., 2012) shows remarkable consistency, with a coefficient of variation of approximately

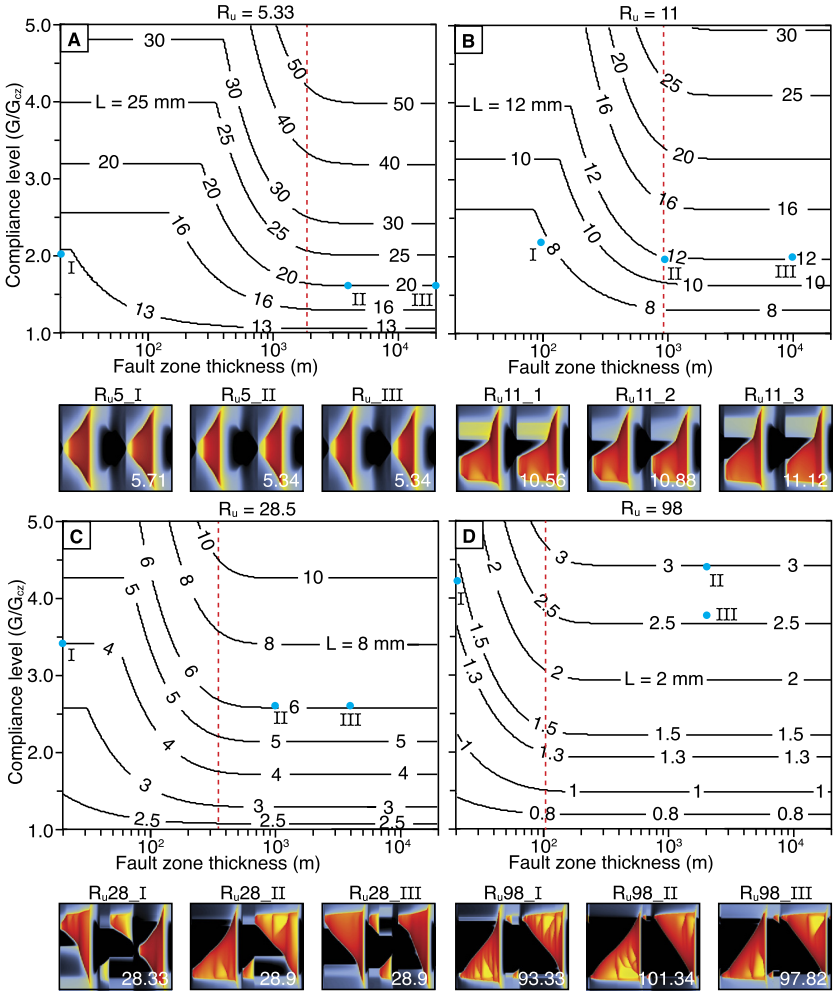


**Fig. 8.** Equivalent sets of fault zone thickness, compliance, and characteristic weakening distance for the same $R_u$ number. a) to d) Relationship among fault zone thickness, compliance, and characteristic weakening distance for $R_u = 5.33$, 11, 28.5 and 98, respectively. The contours are the required characteristic weakening distance, in units of millimeters. The red dash lines indicate the thickness $T = 2h^*$. For each $R_u$ number, the rupture history of three models with different physical units is plotted below each phase diagram. The x- and y-axes of the color plots are time steps and distance, respectively. The white text represents their actual $R_u$ number.

0.37. Our models for a wide range of parameters produce coefficients of variation between zero for strictly periodic earthquakes and above 1 for multi-periodic cycles and random sequences. In this context, the variation of recurrence times at Hokuri Creek is notable, compatible with a parameter regime that exhibits large deviations from time- and slip-predictable recurrence patterns. In turn, such paleo-seismic record can place constraints on the frictional regime of the fault. Although Hokuri Creek is situated in a relatively isolated mature fault of South Island, New Zealand, the recurrence pattern in other tectonic contexts may be strongly influenced by step-overs, neighboring faults, and interactions with the ductile layers. More complex frictional behavior may also contribute to more variable recurrence patterns, including strong-weakening mechanisms during seismic ruptures, and long-term evolution of the fault zone associated with damage evolution, cataclasis, and metamorphism. Simultaneously, the paleo-seismic observations have uncertainties and limitations, making detailed explanations of long-term seismic behavior exceptionally challenging.

Our study shows that the effect of a compliant fault zone on the style of ruptures and recurrence patterns in quasi-dynamic seismic cycles can be approximated by a homogeneous model with physical properties leading to the same $R_u$ number. In contrast, incorporating a compliant zone in fully dynamic simulations leads to a perturbation of the seismic cycle with increasing variability of the hypocenter location (e.g., Huang and Ampuero, 2011; Huang et al., 2014; Thakur et al., 2020). This difference occurs because radiation damping does not capture all the wave-mediated stress transfer. Fault zones create several seismic phases such as trapped waves and head waves (McGuire and Ben-Zion, 2005; Lewis and Ben-Zion, 2010) interacting with the rupture during the coseismic period. Previous studies did not show evidence that trapped and head waves affect the rupture styles or earthquake statistics drastically. However, these studies have been limited to low $R_u$ numbers. The development of off-fault plasticity also affects earthquake recurrence as inelastic deformation dissipates the energy and redistributes the stress field, resulting in more partial ruptures and temporal clustering of earthquakes (Mia et al., 2022).

## 6. Conclusion

We show that the mechanics of faulting implies a strong relationship between the rupture style and recurrence patterns of earthquakes. Fault dynamics depends on the parameter regime, which is determined by the physical properties of the fault zone in and around the seismogenic zone. The presence of a compliant zone reduces the characteristic nucleation size of the seismogenic zone, making it more unstable. However, a similar effect can be obtained in a number of ways in a homogeneous medium, by reducing the characteristic weakening distance of friction, or increasing the effective normal stress. Importantly, there is no particular style

of rupture or recurrence pattern that emerges within a compliant zone that is not also found in a homogeneous elastic medium in our models. Nevertheless, considerable complexity can be found in various parameter regimes linked to specific rupture styles and recurrence patterns. For example, in our models, pulse-like rupture propagation is always associated with large deviations from the time- and slip-predictable models, with partial ruptures of the seismogenic zones, and with the emergence of aftershocks. Earthquake sequences that appear quasi-periodic in the paleo-seismic record are compatible with seismic cycles with full and partial ruptures of the seismogenic zone with crack-like or pulse-like ruptures. We conclude that long-term paleo-seismic records inform earthquake physics beyond seismic hazards and fault activity, also providing fundamental constraints into the fault properties and the frictional regime.

## CRediT authorship contribution statement

Conception and design of study: Shiying Nie, Sylvain Barbot; Analysis of data: Shiying Nie; Drafting the manuscript: Shiying Nie, Sylvain Barbot.

All persons who meet authorship criteria are listed as authors, and all authors certify that they have participated sufficiently in the work to take public responsibility for the content, including participation in the concept, design, analysis, writing, or revision of the manuscript. Furthermore, each author certifies that this material or similar material has not been and will not be submitted to or published in any other publication before its appearance in the Earth and Planetary Science Letter.

## Declaration of competing interest

The authors declare that they have no known competing financial interests or personal relationships that could have appeared to influence the work reported in this paper.

## Acknowledgements

This study is supported in part by the National Science Foundation under award number EAR-1848192. We thank the editor and two anonymous reviewers for their constructive comments.

## Appendix A. Governing equations and non-dimensional parameters

The equations that govern the quasi-dynamic evolution of slip on the fault come about from the balance between shear stress and frictional resistance. The stress evolution satisfies the constitutive relationship of Equation (3), providing

$$\frac{\dot\tau}{\tau}=\frac{a}{\mu_0}\frac{\dot V}{V}+\frac{b}{\mu_0}\frac{\dot\theta}{\theta}\,, \tag{A1}$$

where the terms are defined in the main text. The elastic interactions must conserve momentum, leading to

$$\dot\tau=\int_{-\infty}^{\infty}K(x_3;y_3)\,(V(y_3)-V_L)\,\mathrm{d}y_3-G_{cz}\frac{\dot V}{2V_s}\,, \tag{A2}$$

where $V_L$ is the loading rate. For convenience, we operate the change of variable $\Omega=V\theta/L$, so that the stress evolution satisfies

$$\frac{\dot\tau}{\tau}=\frac{a-b}{\mu_0}\frac{\dot V}{V}+\frac{b}{\mu_0}\frac{\dot\Omega}{\Omega}\,, \tag{A3}$$

making the steady-state velocity dependence on $a-b$ appearing clearly. This gives rise to the governing equation

$$(a-b)\bar\sigma\frac{\mu}{\mu_0}\frac{\dot V}{V}+b\bar\sigma\frac{\mu}{\mu_0}\frac{\dot\Omega}{\Omega}=K*(V-V_L)-\frac{G}{2V_s}\dot V \tag{A4}$$

where $*$ is the convolution operator, coupled to the evolution law

$$\dot\Omega=\frac{V}{L}(1-\Omega)+\frac{\dot V}{V}\Omega\,. \tag{A5}$$

The stress interaction kernel $K(x_3,y_3)$ describes the shear stress on the fault plane at depth $x_3$ due to a line dislocation at depth $y_3$ in the presence of a compliant fault zone of total thickness $T$ and rigidity $G_{cz}$ surrounded by country rocks of rigidity $G$, and is given in conditions of anti-plane strain by the infinite series

$$K(x_3;y_3;G,G_{cz},T)=\\ \frac{G_{cz}}{2\pi}\left[\frac{1}{(x_3-y_3)^2}-2\sum_{m=1}^{\infty}\left(\frac{G-G_{cz}}{G+G_{cz}}\right)^m\frac{(x_3-y_3)^2-(mT)^2}{[(x_3-y_3)^2+(mT)^2]^2}\right]. \tag{A6}$$

The non-dimensional parameters that control the rupture style emerge from a dimensional analysis of the governing equations (A4) to (A6). We scale the coordinate system by the width of the seismogenic zone and the time scale with the characteristic time of weakening, giving rise to

$$\begin{aligned} &x_3=Wx_3'; \quad y_3=Wy_3'\\ &V=V_{\mathrm{L}}V'; \quad \frac{\partial}{\partial t}=\frac{V_{\mathrm{L}}}{L}\frac{\partial}{\partial t'}\,. \end{aligned} \tag{A7}$$

The stress kernel has dimensions scaling with rigidity over square-meters, so we define the dimensionless stress kernel as

$$K=-\frac{G_{cz}}{W^2}K'\,, \tag{A8}$$

where the minus sign indicates that fault slip is associated with a local reduction of stress. This leads to the following expression for the dimensionless stress interaction kernel

$$K'\left(x_3',y_3';\frac{G}{G_{cz}},\frac{T}{W}\right)=\\ \frac{1}{2\pi}\left[\frac{1}{(x_3'-y_3')^2}\right.\\ \left.-2\sum_{m=1}^{\infty}\left(\frac{G/G_{cz}-1}{G/G_{cz}+1}\right)^m\frac{(x_3'-y_3')^2-(mT/W)^2}{[(x_3'-y_3')^2+(mT/W)^2]^2}\right]. \tag{A9}$$

With this change of dynamic variables, the governing equation becomes

$$\frac{\dot V'}{V'}=\frac{1}{R_u^{\mathrm{h}}}\frac{G_{cz}}{G}\frac{\mu_0}{\mu}K'*(V'-1)+\frac{1}{R_b}\frac{\dot\Omega}{\Omega}+\frac{\mu_0}{\mu}\frac{\dot V'}{V'_{\mathrm{th}}} \tag{A10}$$

coupled to an evolution law that contains no physical parameters,

$$\dot\Omega=V'(1-\Omega)+\frac{\dot V'}{V'}\Omega\,, \tag{A11}$$

where the time derivative is with respect to non-dimensional time $t'$. This derivation highlights the controlling non-dimensional parameters. The Dieterich-Ruina-Rice number for a homogeneous medium is given by

$$R_u^{\mathrm{h}}=\frac{W}{L}\frac{(b-a)\bar\sigma}{G}\,, \tag{A12}$$

and controls the elastic interactions. The other non-dimensional number

$$R_b = \frac{b-a}{b}\,, \tag{A13}$$

controls the degree of weakening. The threshold velocity for radiation damping is given by

$$V_{\rm th} = V_L V'_{\rm th} = 2V_s \frac{(b-a)\bar{\sigma}}{G}\,. \tag{A14}$$

The non-dimensional parameters of Equations (A12)-(A14) appear for a homogeneous elastic domain (Barbot, 2019b). The presence of a compliant zone adds two more non-dimensional parameters: the ratio of rigidity $G/G_{cz}$ and the aspect ratio $T/W$, both affecting some aspects of the elastic interactions. This justifies our exploration of these ratios in Figs. 2–8. As we show in the following Appendix, the effect of the compliance ratio and the fault zone thickness can be incorporated into a modified Dieterich-Ruina-Rice number that accounts for the fault zone structure, reducing the number of controlling variables accordingly.

## Appendix B. Dieterich-Ruina-Rice number for a compliant fault zone

We seek a representation of the Dieterich-Ruina-Rice number that incorporates the effect of the fault zone structure. As the compliant zone thickness and rigidity intervene in the elastic interactions through a convolution, it is useful to consider the corresponding term in the Fourier domain. Using the convolution theorem of the Fourier transform, the stress evolution in the Fourier domain is given by

$$\dot{\hat{\tau}} = \hat{K}(\hat{V} - \hat{V}_L) - G_{cz}\frac{\dot{\hat{V}}}{2V_s}\,, \tag{A15}$$

where a hat represents the Fourier transform of the respective field. The stress interaction kernel has the closed-form solution (Idini and Ampuero, 2020)

$$\hat{K}(k_3) = -G_{cz}\pi k_3 \coth\left[\pi\, T k_3 + \operatorname{arctanh}\frac{G_{cz}}{G}\right] \tag{A16}$$

for a compliant zone of total thickness $T$ and rigidity $G_{cz}$ surrounded by country rocks of rigidity $G$, where $k_3$ is the wavenumber associated with the vertical axis. Comparing with the analytic solution for the case of a homogeneous medium

$$\hat{H}(k_3) = -G\pi k_3 \tag{A17}$$

underlines the wavelength dependence of the effective rigidity

$$\hat{G}(k_3) = G_{cz}\coth\left[\pi\, T k_3 + \operatorname{arctanh}(G_{cz}/G)\right], \tag{A18}$$

such that $\hat{K}(k_3) = -\hat{G}(k_3)\pi k_3$. The effective rigidity varies smoothly between the rigidity of the compliant zone and that of the country rocks

$$\begin{aligned} \lim_{k_3\to 0}\hat{G} &= G \\ \lim_{k_3\to\infty}\hat{G} &= G_{cz} \end{aligned} \tag{A19}$$

as long-wavelength and short-wavelength asymptotic solutions, respectively. The Dieterich-Ruina-Rice number is defined as the size of the velocity-weakening region scaled by a characteristic nucleation size as $R_u = W/h^*$. We then evaluate the effective rigidity at the wavelength of nucleation (Kaneko et al., 2011)

$$\begin{aligned} \hat{G}^* &= \hat{G}(1/h^*) \\ &= G_{cz}\coth\left[\pi\, T/h^* + \operatorname{arctanh}\frac{G_{cz}}{G}\right] \\ &= G_{cz}\coth\left[\pi\, R_u\frac{T}{W} + \operatorname{arctanh}\frac{G_{cz}}{G}\right] \end{aligned} \tag{A20}$$

Finally, we redefine the Dieterich-Ruina-Rice number with the effective rigidity

$$R_u = \frac{W}{L}\frac{(b-a)\bar{\sigma}}{G^*}\,. \tag{A21}$$

This provides the transcendental equation for the $R_u$ number used in Equation (8)

$$R_u \coth\left[\pi\, R_u\frac{T}{W} + \operatorname{arctanh}\frac{G_{cz}}{G}\right] = \frac{W}{L}\frac{(b-a)\bar{\sigma}}{G_{cz}}\,, \tag{A22}$$

which is affected by the compliance ratio and the relative thickness of the compliant zone. To better explain our numerical findings in Fig. 2, we substitute the constant $\pi$ in Equation (A22) for a parameter $\lambda = \pi/4$ that better captures the observed nucleation size of earthquake ruptures.

## Appendix C. Supplementary material

Supplementary material related to this article can be found online at https://doi.org/10.1016/j.epsl.2022.117593.

## References


Abdelmeguid, M., Ma, X., Elbanna, A., 2019. A novel hybrid finite element-spectral boundary integral scheme for modeling earthquake cycles: application to rate and state faults with low-velocity zones. J. Geophys. Res. 124 (12), 12,854–12,881.

Agnon, A., 2014. Pre-instrumental earthquakes along the dead sea rift. In: Dead Sea Transform Fault System: Reviews. Springer, pp. 207–261.

Bao, H., Ampuero, J.-P., Meng, L., Fielding, E.J., Liang, C., Milliner, C.W., Feng, T., Huang, H., 2019. Early and persistent supershear rupture of the 2018 magnitude 7.5 Palu earthquake. Nat. Geosci. 12 (3), 200–205. https://doi.org/10.1038/s41561-018-0297-z.

Barbot, S., 2019a. Modulation of fault strength during the seismic cycle by grain-size evolution around contact junctions. Tectonophysics 765, 129–145. https://doi.org/10.1016/j.tecto.2019.05.004.

Barbot, S., 2019b. Slow-slip, slow earthquakes, period-two cycles, full and partial ruptures, and deterministic chaos in a single asperity fault. Tectonophysics 768, 228,171. https://doi.org/10.1016/j.tecto.2019.228171.

Barbot, S., 2020. Frictional and structural controls of seismic super-cycles at the Japan trench. Earth Planets Space 72 (63). https://doi.org/10.1186/s40623-020-01185-3.

Barbot, S., 2021. A spectral boundary-integral method for quasi-dynamic ruptures of multiple parallel faults. Bull. Seismol. Soc. Am. 111 (3), 1614–1630.

Barbot, S., Fialko, Y., Sandwell, D., 2008. Effect of a compliant fault zone on the inferred earthquake slip distribution. J. Geophys. Res. 113 (B6). https://doi.org/10.1029/2007JB005256.

Barbot, S., Fialko, Y., Sandwell, D., 2009. Three-dimensional models of elasto-static deformation in heterogeneous media, with applications to the eastern California shear zone. Geophys. J. Int. 179 (1), 500–520. https://doi.org/10.1111/j.1365-246X.2009.04194.x.

Beroza, G.C., Mikumo, T., 1996. Short slip duration in dynamic rupture in the presence of heterogeneous fault properties. J. Geophys. Res. 101 (B10), 22,449–22,460.

Berryman, K.R., Cochran, U.A., Clark, K.J., Biasi, G.P., Langridge, R.M., Villamor, P., 2012. Major earthquakes occur regularly on an isolated plate boundary fault. Science 336 (6089), 1690–1693.

Bollinger, L., Klinger, Y., Tapponnier, P., Gaudemer, Y., Tiwari, D., 2013. Estimating the return times of great Himalayan earthquakes in eastern Nepal: evidence from the Patu and Bardibas strands of the Main Frontal Thrust. Nat. Geosci. 6, 71–76.

Bufe, C.G., Harsh, P.W., Burford, R.O., 1977. Steady-state seismic slip–a precise recurrence model. Geophys. Res. Lett. 4 (2), 91–94.

Byerlee, J., 1978. Friction of rock. Pure Appl. Geophys. 116, 615–626.

Chen, Q., Freymueller, J.T., 2002. Geodetic evidence for a near-fault compliant zone along the San Andreas fault in the San Francisco bay area. Bull. Seismol. Soc. Am. 92 (2), 656–671.

Chen, Y., Liu, M., Luo, G., 2020. Complex temporal patterns of large earthquakes: Devil's staircases. Bull. Seismol. Soc. Am. 110 (3), 1064–1076. https://doi.org/10.1785/0120190148.
Chester, F., Logan, J.M., 1986. Implications for mechanical properties of brittle faults from observations of the Punchbowl fault zone, California. Pure Appl. Geophys. 124 (1), 79–106.
Chester, F.M., Evans, J.P., Biegel, R.L., 1993. Internal structure and weakening mechanisms of the San Andreas fault. J. Geophys. Res. 98 (B1), 771–786.
Cochran, E.S., Li, Y.-G., Shearer, P.M., Barbot, S., Fialko, Y., Vidale, J.E., 2009. Seismic and geodetic evidence for extensive, long-lived fault damage zones. Geology 37 (4), 315–318.
Day, S.M., 1982. Three-dimensional finite difference simulation of fault dynamics: rectangular faults with fixed rupture velocity. Bull. Seismol. Soc. Am. 72 (3), 705–727.
Day, S.M., Dalguer, L.A., Lapusta, N., Liu, Y., 2005. Comparison of finite difference and boundary integral solutions to three-dimensional spontaneous rupture. J. Geophys. Res. 110 (B12307).
Dieterich, J.H., 1979. Modeling of rock friction: 1. Experimental results and constitutive equations. J. Geophys. Res., Solid Earth 84 (B5), 2161–2168.
Dolan, J.F., McAuliffe, L.J., Rhodes, E.J., McGill, S.F., Zinke, R., 2016. Extreme multi-millennial slip rate variations on the Garlock fault, California: strain supercycles, potentially time-variable fault strength, and implications for system-level earthquake occurrence. Earth Planet. Sci. Lett. 446, 123–136. https://doi.org/10.1016/j.epsl.2016.04.011.
Duan, B., 2008. Effects of low-velocity fault zones on dynamic ruptures with nonelastic off-fault response. Geophys. Res. Lett. 35 (4).
Dunham, E.M., Archuleta, R.J., 2004. Evidence for a supershear transient during the 2002 Denali fault earthquake. Bull. Seismol. Soc. Am. 94 (6B), S256–S268. https://doi.org/10.1785/0120040616.
Ellsworth, W., Beroza, G., 1995. Seismic evidence for an earthquake nucleation phase. Science 268 (5212), 851–855. https://doi.org/10.1126/science.268.5212.851.
Erickson, B.A., Dunham, E.M., Khosravifar, A., 2017. A finite difference method for off-fault plasticity throughout the earthquake cycle. J. Mech. Phys. Solids 109, 50–77.
Fialko, Y., 2004. Space geodetic constraints on the structure and properties of compliant damage zones around major crustal faults. In: AGU Fall Meeting Abstracts, vol. 2004, p. S32B-02.
Fialko, Y., Sandwell, D., Agnew, D., Simons, M., Shearer, P., Minster, B., 2002. Deformation on nearby faults induced by the 1999 Hector Mine earthquake. Science 297, 1858–1862. https://doi.org/10.1126/science.1074671.
Freed, A.M., Lin, J., 2001. Delayed triggering of the 1999 Hector Mine earthquake by viscoelastic stress transfer. Nature 441, 180–183.
Fukuyama, E., Mikumo, T., 2007. Slip-weakening distance estimated at near-fault stations. Geophys. Res. Lett. 34 (9). https://doi.org/10.1029/2006GL029203.
Gauriau, J., Dolan, J.F., 2021. Relative structural complexity of plate-boundary fault systems controls incremental slip-rate behavior of major strike-slip faults. Geochem. Geophys. Geosyst. 22 (11), e2021GC009,938. https://doi.org/10.1029/2021GC009938.
Goldfinger, C., Nelson, C.H., Johnson, J.E., Shipboard Scientific Party, 2003. Holocene earthquake records from the Cascadia subduction zone and northern San Andreas fault based on precise dating of offshore turbidites. Annu. Rev. Earth Planet. Sci. 31 (1), 555–577.
Goldfinger, C., Ikeda, Y., Yeats, R.S., Ren, J., 2013. Superquakes and supercycles. Seismol. Res. Lett. 84 (1), 24–32. https://doi.org/10.1785/0220110135.
Gomberg, J., Johnson, P., 2005. Dynamic triggering of earthquakes. Nature 437 (7060), 830. https://doi.org/10.1038/437830a.
Hamiel, Y., Fialko, Y., 2007a. Structure and mechanical properties of faults in the North Anatolian Fault system from InSAR observations of coseismic deformation due to the 1999 Izmit (Turkey) earthquake. J. Geophys. Res. 112 (B07412). https://doi.org/10.1029/2006JB004777.
Hamiel, Y., Fialko, Y., 2007b. Structure and mechanical properties of faults in the North Anatolian Fault system from insar observations of coseismic deformation due to the 1999 Izmit (Turkey) earthquake. J. Geophys. Res. 112 (B7).
Harris, R.A., Day, S.M., 1997. Effects of a low-velocity zone on a dynamic rupture. Bull. Seismol. Soc. Am. 87 (5), 1267–1280.
Heaton, T.H., 1990. Evidence for and implications of self-healing pulses of slip in earthquake rupture. Phys. Earth Planet. Inter. 64 (1), 1–20.
Huang, Y., 2018. Earthquake rupture in fault zones with along-strike material heterogeneity. J. Geophys. Res. 123 (11), 9884–9898. https://doi.org/10.1029/2018JB016354.
Huang, Y., Ampuero, J.-P., 2011. Pulse-like ruptures induced by low-velocity fault zones. J. Geophys. Res. 116 (B12). https://doi.org/10.1029/2011JB008684.
Huang, Y., Ampuero, J.-P., Helmberger, D.V., 2014. Earthquake ruptures modulated by waves in damaged fault zones. J. Geophys. Res. 119 (4), 3133–3154.
Idini, B., Ampuero, J.-P., 2020. Fault-zone damage promotes pulse-like rupture and back-propagating fronts via quasi-static effects. Geophys. Res. Lett. 47 (23), e2020GL090,736. https://doi.org/10.1029/2020GL090736.
Kaneko, Y., Ampuero, J.-P., Lapusta, N., 2011. Spectral-element simulations of long-term fault slip: effect of low-rigidity layers on earthquake-cycle dynamics. J. Geophys. Res. 116 (B10).
Kato, N., 2014. Deterministic chaos in a simulated sequence of slip events on a single isolated asperity. Geophys. J. Int. 198 (2), 727–736.
King, G.C.P., Stein, R.S., Lin, J., 1994. Static stress changes and the triggering of earthquakes. Bull. Seismol. Soc. Am. 84 (3), 935–953.
Klinger, Y., Etchebes, M., Tapponnier, P., Narteau, C., 2011. Characteristic slip for five great earthquakes along the Fuyun fault in China. Nat. Geosci. 4 (6), 389–392.
Lambert, V., Lapusta, N., Perry, S., 2021. Propagation of large earthquakes as self-healing pulses or mild cracks. Nature 591 (7849), 252–258.
Lapusta, N., Rice, J.R., 2003. Nucleation and early seismic propagation of small and large events in a crustal earthquake model. J. Geophys. Res. 108 (B4).
Leeman, J., Saffer, D., Scuderi, M., Marone, C., 2016. Laboratory observations of slow earthquakes and the spectrum of tectonic fault slip modes. Nat. Commun. 7, 11,104. https://doi.org/10.1038/ncomms11104.
Lewis, M.A., Ben-Zion, Y., 2010. Diversity of fault zone damage and trapping structures in the Parkfield section of the San Andreas fault from comprehensive analysis of near fault seismograms. Geophys. J. Int. 183 (3), 1579–1595.
Li, Y.-G., Aki, K., Adams, D., Hasemi, A., Lee, W.H., 1994. Seismic guided waves trapped in the fault zone of the Landers, California, earthquake of 1992. J. Geophys. Res. 99 (B6), 11,705–11,722.
Lyakhovsky, V., Ben-Zion, Y., Agnon, A., 2001. Earthquake cycle, fault zones, and seismicity patterns in a rheologically layered lithosphere. J. Geophys. Res. 106, 4103–4120.
Marco, S., Klinger, Y., 2014. Review of on-fault palaeoseismic studies along the dead sea fault. In: Dead Sea Transform Fault System: Reviews. Springer, pp. 183–205.
Marone, C., Kilgore, B., 1993. Scaling of the critical slip distance for seismic faulting with shear strain in fault zones. Nature 362, 618–620. https://doi.org/10.1038/362618a0.
McGuire, J., Ben-Zion, Y., 2005. High-resolution imaging of the bear valley section of the San Andreas fault at seismogenic depths with fault-zone head waves and relocated seismicity. Geophys. J. Int. 163 (1), 152–164.
Mei, C., Barbot, S., Wu, W., 2021. Period-multiplying cycles at the transition between stick-slip and stable sliding and implications for the Parkfield period-doubling tremors. Geophys. Res. Lett. 48 (7), e2020GL091,807. https://doi.org/10.1029/2020gl091807.
Mei, C., Barbot, S., Jia, Y., Wu, W., 2022. Experimental evidence for multiple controls on fault stability and rupture dynamics. Earth Planet. Sci. Lett. 577, 117252.
Mia, M.S., Abdelmeguid, M., Elbanna, A.E., 2022. Spatio-temporal clustering of seismicity enabled by off-fault plasticity. Geophys. Res. Lett., e2021GL097601.
Moernaut, J., et al., 2018. Larger earthquakes recur more periodically: new insights in the megathrust earthquake cycle from lacustrine turbidite records in South-central Chile. Earth Planet. Sci. Lett. 481, 9–19.
Montési, L.G., 2004. Controls of shear zone rheology and tectonic loading on post-seismic creep. J. Geophys. Res., Solid Earth 109 (B10).
Nelson, A.R., Kelsey, H.M., Witter, R.C., 2006. Great earthquakes of variable magnitude at the Cascadia subduction zone. Quat. Res. 65 (3), 354–365.
Nie, S., Barbot, S., 2021. Seismogenic and tremorgenic slow slip near the stability transition of frictional sliding. Earth Planet. Sci. Lett. 569, 117,037. https://doi.org/10.1016/j.epsl.2021.117037.
Nishikawa, T., Matsuzawa, T., Ohta, K., Uchida, N., Nishimura, T., Ide, S., 2019. The slow earthquake spectrum in the Japan Trench illuminated by the S-net seafloor observatories. Science 365 (6455), 808–813. https://doi.org/10.1126/science.aax5618.
Nocquet, J.-M., et al., 2017. Supercycle at the Ecuadorian subduction zone revealed after the 2016 Pedernales earthquake. Nat. Geosci. 10 (2), 145. https://doi.org/10.1038/ngeo2864.
Obara, K., Kato, A., 2016. Connecting slow earthquakes to huge earthquakes. Science 353 (6296), 253–257. https://doi.org/10.1126/science.aaf1512.
Omori, F., 1894. On the after-shocks of earthquakes. J. Coll. Sci., Imp. Univ., Japan 7, 111–200.
Patton, J.R., et al., 2015. A 6600 year earthquake history in the region of the 2004 Sumatra-Andaman subduction zone earthquake. Geosphere 11 (6), 2067–2129. https://doi.org/10.1130/GES01066.1.
Pelties, C., Huang, Y., Ampuero, J.-P., 2015. Pulse-like rupture induced by three-dimensional fault zone flower structures. Pure Appl. Geophys. 172 (5), 1229–1241. https://doi.org/10.1007/s00024-014-0881-0.
Peng, Z., Gomberg, J., 2010. An integrated perspective of the continuum between earthquakes and slow-slip phenomena. Nat. Geosci. 3 (9), 599. https://doi.org/10.1038/ngeo940.
Perfettini, H., Avouac, J.-P., 2004. Postseismic relaxation driven by brittle creep: a possible mechanism to reconcile geodetic measurements and the decay rate of aftershocks, application to the chi-chi earthquake, Taiwan. J. Geophys. Res., Solid Earth 109 (B2).
Philibosian, B., Meltzner, A.J., 2020. Segmentation and supercycles: a catalog of earthquake rupture patterns from the Sumatran Sunda Megathrust and other well-studied faults worldwide. Quat. Sci. Rev. 241, 106,390. https://doi.org/10.1016/j.quascirev.2020.106390.
Philibosian, B., et al., 2017. Earthquake supercycles on the Mentawai segment of the Sunda megathrust in the seventeenth century and earlier. J. Geophys. Res. 122 (1), 642–676. https://doi.org/10.1002/2016JB013560.

Ran, Y., Xu, X., Wang, H., Chen, W., Chen, L., Liang, M., Yang, H., Li, Y., Liu, H., 2019. Evidence of characteristic earthquakes on thrust faults from paleo-rupture behavior along the Longmenshan fault system. Tectonics 38 (7), 2401–2410.

Reid, H.F., 1910. The mechanics of the earthquake, the California Earthquake of April 18, 1906. Report of the State Earthquake Investigation Commission.

Rice, J.R., Ruina, A.L., 1983. Stability of steady frictional slipping. J. Appl. Mech. 50, 343–349. https://doi.org/10.1115/1.3167042.

Rockwell, T.K., Dawson, T.E., Ben-Horin, J.Y., Seitz, G., 2015. A 21-event, 4,000-year history of surface ruptures in the anza seismic gap, San Jacinto Fault, and implications for long-term earthquake production on a major plate boundary fault. Pure Appl. Geophys. 172 (5), 1143–1165.

Ross, Z.E., Trugman, D.T., Azizzadenesheli, K., Anandkumar, A., 2020. Directivity modes of earthquake populations with unsupervised learning. J. Geophys. Res. 125 (2), e2019JB018,299. https://doi.org/10.1029/2019JB018299.

Rubin, C.M., Horton, B.P., Sieh, K., Pilarczyk, J.E., Daly, P., Ismail, N., Parnell, A.C., 2017. Highly variable recurrence of tsunamis in the 7,400 years before the 2004 Indian Ocean Tsunami. Nat. Commun. 8, 16,019.

Ruina, A., 1983. Slip instability and state variable friction laws. J. Geophys. Res. 88 (B12), 10,359–10,370.

Sapkota, S., Bollinger, L., Klinger, Y., Tapponnier, P., Gaudemer, Y., Tiwari, D., 2013. Primary surface ruptures of the great Himalayan earthquakes in 1934 and 1255. Nat. Geosci. 6 (1), 71–76.

Sawai, Y., 2020. Subduction zone paleoseismology along the Pacific coast of northeast Japan—progress and remaining problems. Earth-Sci. Rev., 103261. https://doi.org/10.1016/j.earscirev.2020.103261.

Scharer, K.M., Yule, D., 2020. A maximum rupture model for the southern San Andreas and San Jacinto Faults, California, derived from paleoseismic earthquake ages: observations and limitations. Geophys. Res. Lett. 47 (15), e2020GL088,532.

Shapiro, N.M., Campillo, M., Stehly, L., Ritzwoller, M.H., 2005. High-resolution surface-wave tomography from ambient seismic noise. Science 307 (5715), 1615–1618.

Shimazaki, K., Nakata, T., 1980. Time-predictable recurrence model for large earthquakes. Geophys. Res. Lett. 7 (4), 279–282.

Sieh, K., 1996. The repetition of large-earthquake ruptures. Proc. Natl. Acad. Sci. 93 (9), 3764–3771. https://doi.org/10.1073/pnas.93.9.3764.

Sieh, K., et al., 2008. Earthquake supercycles inferred from sea-level changes recorded in the corals of West Sumatra. Science 322, 1674–1678. https://doi.org/10.1126/science.1163589.

Sieh, K.E., Jahns, R.H., 1984. Holocene activity of the San Andreas Fault at Wallace Creek, California. Geology 95 (8), 883–896. https://doi.org/10.1130/0016-7606(1984)95<883:HAOTSA>2.0.CO;2.

Sykes, L.R., Menke, W., 2006. Repeat times of large earthquakes: implications for earthquake mechanics and long-term prediction. Bull. Seismol. Soc. Am. 96 (5), 1569–1596. https://doi.org/10.1785/0120050083.

Thakur, P., Huang, Y., Kaneko, Y., 2020. Effects of low-velocity fault damage zones on long-term earthquake behaviors on mature strike-slip faults. J. Geophys. Res. 125 (8), e2020JB019,587. https://doi.org/10.1029/2020JB019587.

Usami, K., Ikehara, K., Kanamatsu, T., McHugh, C.M., 2018. Supercycle in great earthquake recurrence along the Japan Trench over the last 4000 years. Geosci. Lett. 5 (1), 11. https://doi.org/10.1186/s40562-018-0110-2.

Utsu, T., 1961. A statistical study on the occurrence of aftershocks. Geophys. Mag. 30, 521–605.

Veedu, D., Barbot, S., 2016. The Parkfield tremors reveal slow and fast ruptures on the same asperity. Nature 532 (7599), 361–365. https://doi.org/10.1038/nature17190.

Veedu, D.M., Giorgetti, C., Scuderi, M., Barbot, S., Marone, C., Collettini, C., 2020. Bifurcations at the stability transition of earthquake faulting. Geophys. Res. Lett. 47 (19), e2020GL087,985. https://doi.org/10.1029/2020GL087985.

Vidale, J.E., Li, Y.-G., 2003. Damage to the shallow landers fault from the nearby hector mine earthquake. Nature 421 (6922), 524–526.

Wang, Y., Day, S.M., 2017. Seismic source spectral properties of crack-like and pulse-like modes of dynamic rupture. J. Geophys. Res. 122 (8), 6657–6684.

Wang, Y., Day, S.M., Denolle, M.A., 2019. Geometric controls on pulse-like rupture in a dynamic model of the 2015 Gorkha earthquake. J. Geophys. Res. 124 (2), 1544–1568.

Weldon, R., Scharer, K., Fumal, T., Biasi, G., 2004. Wrightwood and the earthquake cycle: what a long recurrence record tells us about how faults work. GSA Today 14 (9), 4–10. https://doi.org/10.1130/1052-5173(2004)014<4:WATECW>2.0.CO;2.

Wesnousky, S.G., 1988. Seismological and structural evolution of strike-slip faults. Nature 335 (6188), 340–343. https://doi.org/10.1038/335340a0.

Wesnousky, S.G., 2006. Predicting the endpoints of earthquake ruptures. Nature 444 (7117), 358–360. https://doi.org/10.1038/nature05275.

Wu, Y., Chen, X., 2014. The scale-dependent slip pattern for a uniform fault model obeying the rate- and state-dependent friction law. J. Geophys. Res. 119 (6), 4890–4906. https://doi.org/10.1002/2013JB010779.

Youngs, R.R., Coppersmith, K.J., 1985. Implications of fault slip rates and earthquake recurrence models to probabilistic seismic hazard estimates. Bull. Seismol. Soc. Am. 75 (4), 939–964.